ASME Journal of Fluids Engineering
Online journal at:
https://asmedigitalcollection.asme.org/fluidsengineering

Development of a Novel Freezing-Levitation System for Controlled Contact-Free Generation of Supercooled Droplets

MD Sohaib Bin Sarwar
Department of Mechanical Engineering,
The City College of New York,
New York, NY 10031

Haipeng Zhang
Department of Mechanical Engineering,
The City College of New York,
New York, NY 10031

Yang Liu[1]
Department of Mechanical Engineering,
The City College of New York,
New York, NY 10031
e-mail: yliu7@ccny.cuny.edu

Supercooled droplets are liquid droplets existing below their equilibrium freezing point without solidification, which occur widely in natural and industrial environments and play critical roles in atmospheric science, cryopreservation, and aviation safety. Supercooled droplets exhibit unique characteristics, such as rapid freezing triggered by impingement or other disturbances. To better reveal the dynamic and thermal processes experienced by supercooled droplets, controlled laboratory generation of supercooled droplets is essential for systematic investigations. In this study, we developed a novel freezing-levitation system to produce supercooled droplets without direct contact or support. Both high-speed imaging and infrared thermography were applied to characterize the supercooling process and the subsequent droplet impinging dynamics. Different types of water droplets, i.e., de-ionized-water and tap-water, were used in the experiments and compared in terms of their supercooling and freezing behaviors. The observations revealed that, while a clear recalescence event occurred for the tap water droplet during supercooling, the de-ionized water droplet remained in a liquid state for an extended period. Droplet impact experiments showed that both supercooled and nonsupercooled droplets spread similarly during the inertial stage. However, their retraction varied, i.e., the supercooled droplet showed suppressed recoil, while the nonsupercooled droplet underwent full capillary retraction before freezing. These findings demonstrate that the developed freezing-levitation system can consistently and precisely produce supercooled droplets that can offer reliable experimental conditions in examining the thermal and hydrodynamic features of supercooled droplets in both static and dynamic environments.
[DOI: 10.1115/1.4072162]

Keywords: supercooled droplet, supercooling degree, acoustic levitation, recalescence, droplet impact, freezing

1 Introduction

Under equilibrium conditions, pure water freezes at 0 °C under atmospheric pressure. However, in practice, liquid water may remain unfrozen even when cooled below this temperature if ice nucleation does not occur. In that case, the droplet exists in a metastable supercooled state, whose persistence depends on nucleation kinetics as well as on the presence of impurities, interfaces, and other factors that can facilitate the formation of a critical ice nucleus [1,2]. Once nucleation is initiated, the freezing of a supercooled droplet can proceed rapidly and is often characterized by several stages, i.e., ice nucleation, rapid crystal growth accompanied by recalescence, and subsequent solidification of the remaining liquid [1,3]. Disturbances emerge when a droplet impacts a solid substrate, which can provide favorable conditions for heterogeneous nucleation through contact with the solid surfaces, defects, trapped air, or contact line disturbances [4–6]. Recent studies have further clarified that, although the early spreading stage of droplet impact on cold substrates is primarily governed by inertia and capillarity, the subsequent retraction, contact time, and freezing behavior become increasingly sensitive to thermal conditions, viscosity variation, and phase-change kinetics. For example, recent experimental and numerical studies have shown that the temperature difference between the impinging droplet and the cold substrate can strongly affect retraction and freezing progression while exerting comparatively weaker influence on the maximum spreading diameter during the initial inertial stage [7–10]. This process is closely related to the onset of ice accretion on aircraft or wind turbine surfaces under icing conditions, which has been widely recognized as a severe weather hazard in these fields [11]. Beyond these, the freezing and impact behavior of supercooled droplets is also relevant to a broad range of applications, such as atmospheric science, anti-/de-icing technologies, cryopreservation, and phase-change heat transfer processes [1,3,5,12–15].

Fluids Engineering Division Summer Meeting (FEDSM) 2025—Philadelphia, PA. FEDSM2025.
[1]Corresponding author.
Contributed by the Fluids Engineering Division of ASME for publication in the Journal of Fluids Engineering. Manuscript received December 16, 2025; final manuscript received June 11, 2026; published online July 15, 2026. Assoc. Editor: John Palmore Jr.

It is well established that the temperature of a supercooled droplet, or its degree of supercooling, plays a critical role in governing both its dynamic behavior and freezing process [16,17]. Even at temperatures below the equilibrium freezing point, relatively small variations in droplet temperature can lead to significantly different nucleation behavior and impact outcomes, including the onset time of freezing, the occurrence of recalescence, the degree of spreading and retraction, and the final frozen morphology. Consequently, experimental investigations require the generation of supercooled droplets with precisely controlled temperatures and high repeatability. Despite this need, producing well-controlled supercooled droplets remains experimentally challenging. Several approaches have been developed, most notably cooling droplets during free fall in air or cooling droplets in a supported configuration [1,5,6,15]. In the free-fall method, a droplet is released from a reservoir and allowed to pass through a cooling channel containing cooling elements, such as dry ice [1,5]. However, the achievable cooling time is constrained by the droplet's falling velocity, and reaching lower temperatures typically necessitates increasing the falling height, an approach that is often impractical in laboratory environments with limited vertical space. Moreover, increasing the falling height inevitably increases the droplet's impact velocity, thereby reducing independent control over droplet temperature and impact conditions. Alternatively, in the supported-supercooling method, a droplet is first formed and held on a needle tip or minimal physical support and subsequently cooled to the desired temperature [6,15]. This approach offers improved control over droplet temperature and initial motion. Nevertheless, the presence of the supporting needle or wire can act as a heterogeneous nucleation site, often triggering premature freezing before the droplet reaches the intended supercooled state.

To address the longstanding challenge of generating supercooled droplets with precisely controlled and repeatable degrees of supercooling, we developed a novel freezing-levitation system that enables contact-free droplet generation, suspension, and cooling. The system consists of two integrated components: an acoustic levitation-based droplet suspension module and a controlled environmental cooling module. Unlike conventional free-fall or supported-droplet approaches, this design eliminates physical contact and decouples droplet temperature control from impact dynamics. In this system, water droplets are generated at the center of an acoustic levitator using a needle tip connected to a syringe pump. When activated, standing acoustic waves produced by an array of transducers trap the droplet in stable suspension [18,19]. The levitator frame incorporates a through-hole that allows the droplet to be released vertically when the acoustic field is turned off, enabling controlled droplet deployment without mechanical interference. The entire apparatus is housed within a temperature-controlled freezer chamber, allowing the levitated droplet to cool uniformly through its surrounding environment. By precisely regulating the levitation duration, droplets can be reproducibly cooled to prescribed target temperatures prior to release.

It should be noted that acoustic levitation may induce internal circulation and acoustic streaming within the droplet, which can influence convective heat transfer and potentially affect the redistribution of dissolved impurities, and thus the supercooling performance. To demonstrate the capabilities of the proposed system, high-speed imaging and infrared thermography were employed to simultaneously capture droplet dynamics and temperature evolution. The thermal measurements were carefully calibrated and validated using a thermocouple, and a theoretical model based on Newton's law of cooling was developed to correlate the droplet temperature with the cooling duration and to provide a quantitative comparison with experimental results [20]. Using this platform, a series of proof-of-concept experiments were performed in which supercooled droplets with prescribed degrees of supercooling were released to impinge on solid substrates. The observations reveal distinct spreading and freezing behaviors that depend sensitively on the initial supercooling level. These results demonstrate that the present freezing-levitation system enables the reliable and repeatable generation of well-controlled supercooled droplets, providing a robust experimental foundation for systematic investigations into the dynamics and freezing mechanisms of supercooled droplets.

2 Materials and Methods

2.1 Materials. Deionized (DI) water and tap water were used as the working fluids to generate supercooled droplets. The physical properties of DI water at atmospheric pressure and room temperature (20 °C) are as follows: density (ρ) is 998 kg/m^3, viscosity (μ) is 1.003×10^{-3} N·s/m^2, and the surface tension coefficient in air (γ) is 0.0728 N/m. When the temperature is reduced to 0 °C, these values change to $\rho = 1000$ kg/m^3, $\mu = 1.788 \times 10^{-3}$ N·s/m^2, and $\gamma = 0.0756$ N/m, respectively [21]. Tap water exhibits thermophysical properties that are very close to those of DI water under the same conditions. In the present experiments, no measurable differences were observed in droplet formation, levitation stability, or cooling behavior between the two fluids, indicating that the system is not overly sensitive to minor dissolved impurities.

In the droplet impingement experiments, aluminum plates (55 mm × 50 mm × 1 mm) with hydrophilic surface coating (Painter's Touch Ultra-Cover 2×, Paint + Primer, Flat Black, Rust-Oleum) were used as substrates. The contact angle was measured using the sessile-drop method, in which a droplet was gently released onto the inclined substrate and allowed to relax completely before measurement. Side-view images of the fully relaxed droplet were then processed to identify the droplet interface and fit the local tangent near the contact line to compute the respective angles, as shown in Fig. 1. The static contact angle of DI water droplets on the coated surface was measured to be approximately 65 deg ± 0.8 deg at room temperature, as shown in Fig. 1(*a*). By using a similar needle-in-the-sessile-drop method as that described in Korhonen et al. [22], the advancing and receding

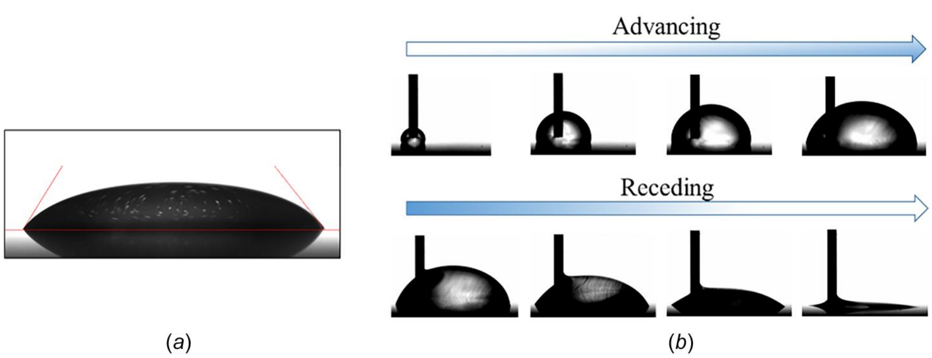

Fig. 1 Measurements of static (*a*), advancing and receding (*b*) contact angles of DI water droplet on the experimental surface

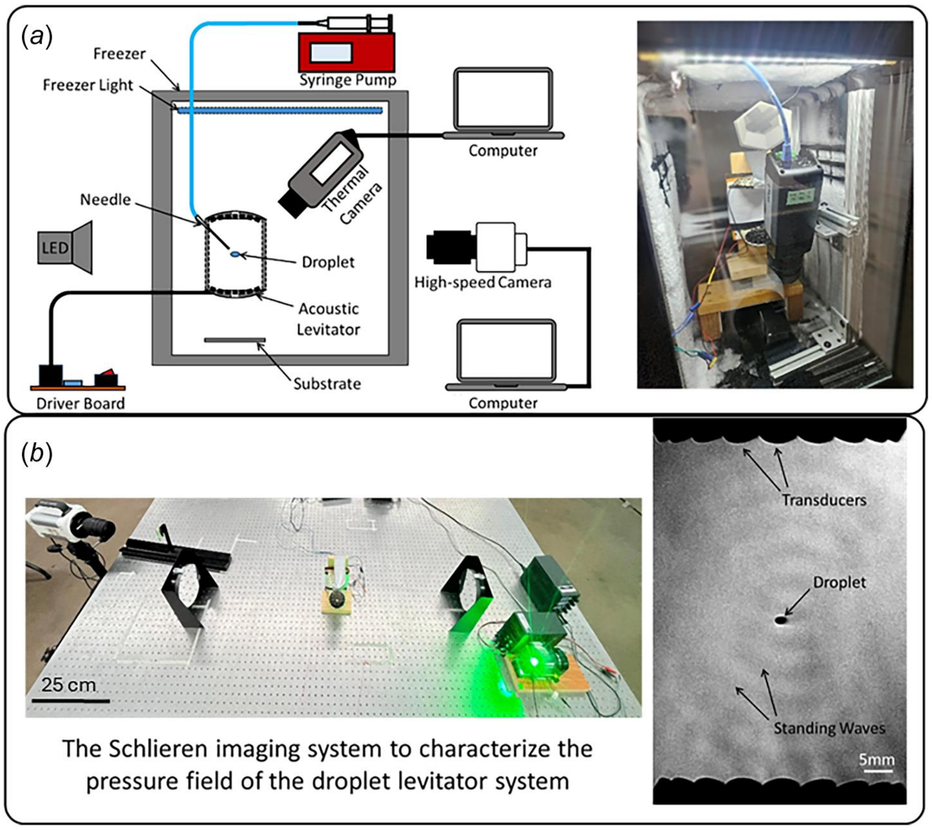

Fig. 2 **(*a*) The layout and experimental setup of the freezing-levitation system and the imaging system and (*b*) the experimental setup of the Schlieren imaging system to characterize the pressure field of the droplet levitator system, and an example image of a droplet suspended by standing waves in the levitator**

angles of water droplets over the surface were also measured as shown in Fig. 1(*b*), with advancing and receding angles being 105 deg $\pm$1.5 deg and 50 deg $\pm$1.2 deg, confirming the strongly hydrophilic nature of the substrate and providing a well-defined baseline for analyzing droplet spreading and freezing behavior. It should be noted that, the reported contact angles are presented as the mean value from $N = 5$ independent trials, with errors of $\pm 0.8°$ for the static contact angle measurements, $\pm$1.5 deg and $\pm$1.2 deg for the advancing and receding contact angle measurements, respectively.

2.2 Experimental Setup and Procedures. The overall layout of the freezing-levitation system developed for generating supercooled droplets is illustrated in Fig. 2. The experimental apparatus consists of two integrated subsystems: (i) a droplet generation and contact-free suspension system and (ii) a temperature-controlled cooling system based on a commercial freezing chamber. As clearly shown in Fig. 2(*a*), the droplet generation and suspension subsystem is built around a custom-designed acoustic levitator comprising a total of 72 ultrasonic transducers operating at 40 kHz, arranged symmetrically on the upper and lower sections of a rigid frame. The upper and lower array surfaces are spaced 7.5 cm apart and each array contains 36 ultrasonic transducers. These transducers are driven by a dedicated control board to produce a stable acoustic standing-wave field at the 9V input voltage. As shown in Fig. 2(*b*), Schlieren imaging is used to visualize the resulting air-density gradients, clearly demonstrating the formation of standing waves capable of trapping small objects in air, including individual water droplets. A Z-type Schlieren arrangement was used to visualize the air-density gradients associated with the acoustic standing-wave field. The Schlieren system was assembled in-house and consisted of 127 mm concave mirrors with a focal length of 1524 mm, a laser light source, and a knife edge placed at the focal point. The Schlieren images were used qualitatively to confirm the standing-wave structure. It should be noted that, the Schlieren image was acquired outside the freezer because of limitations in optical access. The purpose of the Schlieren imaging is to visualize and characterize the pressure field, i.e., the acoustic standing waves, to illustrate the mechanism of droplet trapping. Since the droplet trapping mechanism is the same under room-temperature and freezing conditions, the Schlieren measurement remains representative of the levitation field in the freezing experiments.

A stainless-steel needle (32 G, inner diameter = 0.108 mm) was positioned with its tip aligned at the acoustic pressure node at the center of the levitator to generate droplets directly within the standing-wave field. The needle was connected via flexible tubing filled with de-ionized water or tap water to a 10 mL plastic syringe (inner diameter = 14.5 mm, Vita Needle Company), which was driven by a programable syringe pump (NE-300, New Era Pump Systems, Inc. Farmingdale, NY). The syringe pump operated at a low volumetric flowrate of 0.1 mL/min, allowing a water droplet to grow quasi-statically at the needle tip with negligible inertial effects. Once the droplet reached a critical size, it detached from the needle and was immediately captured by the acoustic field, resulting in stable, contact-free levitation, as shown in Fig. 2.

The key nondimensional groups for the droplet-impact conditions were estimated using the measured droplet diameter and the impact velocity inferred from the release height, which gives an impact velocity of $U_d \approx 1.74\,\mathrm{m/s}$. The Weber, Reynolds, Bond, and Ohnesorge numbers are defined as

$$\mathrm{We} = \frac{\rho U_d^2 D_d}{\gamma} \tag{1}$$

$$\mathrm{Re} = \frac{\rho U_d D_d}{\mu} \tag{2}$$

$$\mathrm{Bo} = \frac{\rho g D_d^2}{\gamma} \quad (3)$$

$$\mathrm{Oh} = \frac{\mu}{\sqrt{\rho \gamma D_d}} \quad (4)$$

Using these definitions, the corresponding values are estimated as We ≈ 120, Re ≈ 2.9×10^3, Bo ≈ 1.2, and Oh ≈ 0.012, indicating an inertia-capillary-dominated regime. These values are of a similar order of magnitude as those reported in prior studies [5].

The entire freezing-levitation apparatus was housed within a freezing chamber equipped with a transparent front door (LSD-60 Household Display Freezer, Ningbo Hicon Industry Technology Co., Ltd.), enabling optical access during experiments. The ambient temperature inside the freezer chamber was monitored and maintained within the range of −7.9 to −8.4 °C. Under these conditions, the levitated droplet was cooled uniformly by the surrounding cold environment over a prescribed cooling duration, *t*, while remaining fully suspended and free from physical contact. After the desired cooling time was reached, the acoustic levitator was switched off, thereby eliminating the standing-wave field. The supercooled droplet was then released under gravity and allowed to fall vertically through an aligned opening located at the center of the lower section of the levitator frame. This design ensured an unobstructed and repeatable release pathway, enabling the droplet to be reliably collected or directed toward a target substrate for subsequent characterization and impingement experiments.

For demonstration purposes, supercooled droplet impingement experiments were conducted inside the freezer chamber using the developed freezing-levitation system. Hydrophilic aluminum substrates, prepared as described previously, were positioned directly beneath the acoustic levitator to serve as impact targets. The vertical falling distance of the supercooled droplet from the center of the levitator to the substrate surface was measured to be 15.4 cm, providing a repeatable and well-defined impact condition. In the present study, both the droplet size and release height were kept fixed. This choice was made because droplets of approximately this size could be trapped most reliably in the acoustic levitation system while still enabling clear optical and infrared measurements, whereas the release height was constrained by the limited vertical space available inside the freezer chamber. All experiments were repeated five times under the same nominal conditions to confirm the consistency of the observed impact and freezing behavior, and representative cases are presented here to highlight the common physical trends. The droplet impact dynamics were captured using a high-speed camera (Phantom VEO 440-L, Vision Research) mounted outside the freezer operating at 10,000 frames per second and viewing the experiment through the transparent front door. Simultaneously, the thermal evolution of the droplet during cooling and impact was monitored at 200 Hz using an infrared camera (FLIR A655sc, FLIR Systems AB) installed inside the freezer chamber. To ensure sufficient illumination and image clarity, a high-intensity light emitting diode (LED) light source (RS-5620, RPS Studio CooLED 200 Studio Light, Dot Line Corp.) with additional optics and mirrors was positioned in front of the freezer door, providing uniform backlighting for high-speed imaging.

2.3 Acoustic Levitation of Droplet. In order to levitate a droplet in the acoustic field, the acoustic radiation force produced by the levitator must overcome the gravity of the droplet. The droplet weight was estimated using a spherical approximation, since the measured aspect ratio D_h/D_v remained close to unity during levitation, indicating only minor deviation from a spherical shape. Accordingly, the droplet volume was approximated as

$$V = \frac{4}{3}\pi r^3 = \frac{\pi D_d^3}{6} \approx 1.41 \times 10^{-8}\, m^3 \quad (5)$$

and the droplet weight was estimated as

$$F_g = mg = \rho V g = \rho \left(\frac{\pi D_d^3}{6}\right) g \approx 1.38 \times 10^{-4} N \quad (6)$$

For a small particle in a standing wave, the acoustic radiation force can be derived from the Gor'kov potential [23]. In 1D form, the axial force is often written as

$$F_z = 4\pi r^3 k E_{\mathrm{ac}} \Phi \sin(2kz) \quad (7)$$

where r is droplet radius, $k = \frac{2\pi}{\lambda}$ is wavenumber, $\lambda = \frac{c}{f}$ is wavelength, E_{ac} is acoustic energy density, Φ is acoustic contrast factor, z is position in standing wave, c is speed of sound, and f is the acoustic wave frequency.

At 40 kHz in air, with $c \approx 343\,\mathrm{m/s}$, $\lambda = \frac{343}{40000} \approx 8.58\,\mathrm{mm}$, therefore $k = \frac{2\pi}{\lambda} \approx 732\,\mathrm{m}^{-1}$.

The maximum force magnitude is approximately

$$F_{\max} \approx 4\pi r^3 k E_{\mathrm{ac}} \mid \Phi \mid \quad (8)$$

For the acoustic energy density, a useful estimate is $E_{\mathrm{ac}} \approx \frac{p_0^2}{4\rho_0 c^2}$, for a standing-wave field, where p_0 is pressure amplitude, $\rho_0 \approx 1.2\,\mathrm{kg/m^3}$ for air, $c \approx 343\,\mathrm{m/s}$, substitute into the force equation

$$F_{\max} \approx \pi r^3 k \left(\frac{p_0^2}{\rho_0 c^2}\right) \mid \Phi \mid \quad (9)$$

In this study, the droplet radius $r = 1.5\,\mathrm{mm} = 1.5 \times 10^{-3}\,\mathrm{m}$, $f = 40\,\mathrm{kHz}$, $k \approx 732\,\mathrm{m}^{-1}$, and acoustic pressure $p_0 \approx 3000\,\mathrm{Pa}$ for a 40 kHz acoustic field, air density $\rho_0 = 1.2\,\mathrm{kg/m^3}$, $c = 343\,\mathrm{m/s}$, $\mid \Phi \mid \approx 1$.

Then

$$F_{\max} \approx 5.0 \times 10^{-4}\,\mathrm{N} \quad (10)$$

Comparing the order of magnitudes between the gravitational force on the droplet and the acoustic radiation force, it is clearly seen that the acoustic radiation force is sufficient to overcome the droplet gravity and keep it suspended in the air.

2.4 Calibration of Temperature Measurement From Infrared Thermal Images. The temperature of the supercooled droplet (T_d) was determined from infrared images recorded by the thermal camera. Prior to the droplet experiments, a calibration procedure was performed to establish a direct relationship between the infrared camera digital count and the actual temperature of water under the same measurement configuration. A plastic container filled with deionized water was placed on an adjustable-height stand inside the freezer chamber. The stand height was carefully adjusted so that the free surface of the water coincided with the vertical position of the levitated droplet in the acoustic levitator, thereby ensuring consistent optical and thermal measurement conditions. The infrared camera recorded the apparent temperature of the water surface in raw digital counts (C, proportional to the thermal radiation received from the measuring surfaces), while a calibrated thermocouple with an accuracy of approximately ±0.1 °C according to the manufacturer's specification (DT304 Apollo IV Digital Temperature Logger, UEi Test Instruments) simultaneously measured the actual water temperature as a reference. The infrared camera data and thermocouple measurements were then correlated using linear regression, and the resulting calibration relationship was used to convert the count numbers (C) recorded in the infrared images into quantitative droplet temperature data throughout this study.

After applying linear fitting to the data, two fitting results were obtained: $T_d = 0.0093\,C - 93.771$ for positive temperature and $T_d = 0.0297\,C - 297.49$ for negative temperature, respectively. These fits appeared in different temperature ranges, suggesting that the change in C followed different trends before and after the water froze due to changes in emissivity. It should be noted that, this calibration is based on the direct empirical relationship between the camera-received radiation signal and the measured water temperature under the present experimental setup. In this sense, the combined effects of emissivity, reflections, surface condition, and surrounding environmental influences are inherently incorporated into the calibration relation.

In addition, because the infrared camera operates in the 7.5–14 μm spectral range, where liquid water is strongly absorbing, the measured infrared signal mainly reflects the apparent surface temperature of the droplet. Based on reported optical properties of water in this wavelength range, the absorption coefficient is typically of the order of 10^2–$10^3 cm^{-1}$, corresponding to an infrared penetration depth of only several to several tens of microns. Therefore, for a sufficiently thick droplet or liquid layer, the contribution from the droplet interior is limited, and the measured signal is dominated by radiation from the surface region. During droplet impact, however, the spreading lamella may become thin enough that the underlying substrate could also influence the measured signal. For the present conditions ($D_0 \approx 3$ mm and We ≈ 120), a simple estimate based on volume conservation gives an average lamella thickness of approximately 0.18 mm (180 μm) at maximum spreading, which remains substantially larger than the infrared penetration depth in water. This suggests that, over most of the spreading droplet area, the infrared signal is still mainly associated with the apparent surface temperature of the water layer. However, because the lamella thickness is not spatially uniform and may become much smaller near the advancing edge or during the late spreading stage, local contributions from the substrate cannot be completely excluded in the thinnest regions.

In the present work, the infrared measurements are primarily used to characterize the overall droplet temperature level and thermal evolution trend during levitation, supercooling, and impingement. A more detailed analysis of local temperature distribution within the droplet, which may be affected by droplet curvature and possible surface-to-bulk temperature differences, is beyond the scope of this study.

2.5 Data Analysis and Image Processing. Custom MATLAB scripts were developed and employed to extract key geometric parameters of droplets from the recorded images, including the size and shape of levitated droplets as well as the spreading diameter (D) and height (H) of droplets on the substrate after impingement [24]. The image processing procedure was designed to be automated and repeatable to minimize user-dependent variability. Briefly, each image containing a droplet was first subjected to automatic contrast enhancement using the *graythresh* function. The processed image was then converted into a binary format using the *imbinarize* function, allowing clear separation of the droplet from the background. Subsequently, the droplet boundary was identified using the *bwtraceboundary* function. For levitated droplets, the detected boundary was used to determine the droplet diameter and overall geometry. For droplets after impingement, the horizontal and vertical extents of the boundary were measured to obtain the spreading diameter (D) and height (H), respectively. Additional geometric parameters, such as the initial droplet diameter (D_d), were obtained using the same image processing workflow to ensure consistency across all measurements in this study.

3 Results and Discussions

3.1 Shape Evolution of Acoustic Levitated Droplet. Figure 3 shows the shape evolution of an acoustically levitated droplet while suspended in the freezer over time, and when released from the levitator. When a droplet is levitated by the acoustic standing-wave field, it experiences compression from the top and bottom, resulting in an ellipsoidal shape, consistent with previous observations [25,26]. During the cooling process, no noticeable influence of temperature on the droplet shape was observed [19].

The droplet image at $t = 0$ s corresponds to the moment when the droplet is introduced into the acoustic levitator and reaches a steady levitation state. As time progresses, the droplet may exhibit mild spinning or oscillatory motion. However, it remains stably trapped at its original location throughout the cooling process. The droplet dimensions in the horizontal and vertical directions were quantified as D_h and D_v, respectively. The corresponding aspect ratio, defined as D_h/D_v, is plotted as a function of time over a representative interval of 10 s in Fig. 3(*a*). The aspect ratio remains nearly constant, indicating that no significant shape deformation occurs during the freezing-levitation process.

The maintained stability of the droplet during levitation is particularly important under freezing conditions, as it indicates that the acoustic trapping force and pressure field remain sufficiently uniform throughout the cooling process. This stability helps preserve a well-defined droplet geometry and controlled thermal history prior to release, both of which are essential for achieving repeatable and physically meaningful supercooled impingement experiments. In particular, stable levitation minimizes unintended disturbances that could alter internal flow, promote premature nucleation, or modify the degree of supercooling before impact. On the other hand, the droplet deformation immediately following release from the acoustic levitator exhibits distinctly different behavior. Figure 3(*b*) summarizes the temporal evolution of droplet shape after release. The droplet image at $t = 0$ s corresponds to the instant at which the acoustic levitator was switched off. Upon

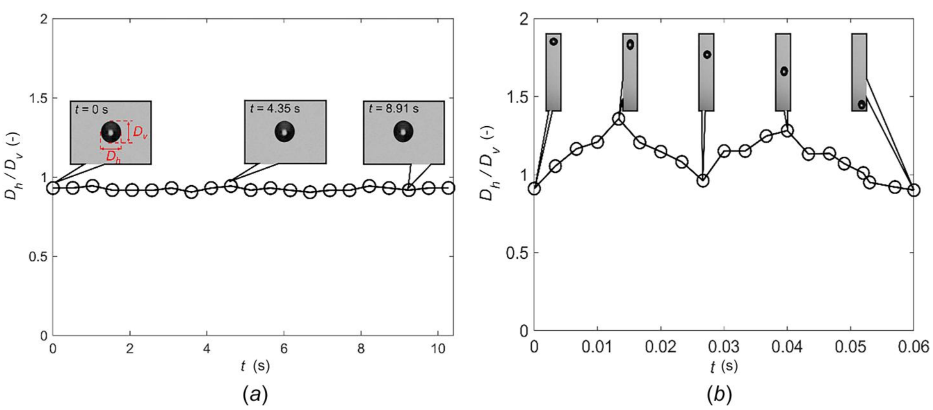

Fig. 3 Shape evolution of an acoustically levitated droplet (*a*) while suspended showing time-sequence images of a droplet suspended in the freezer and aspect ratio of the droplet (D_h/D_v) over time (*t*); and (*b*) after the droplet is released, showing time-sequence images of the droplet falling inside the freezer and the corresponding temporal variation of the droplet aspect ratio, D_h/D_v

removal of the standing-wave field, the droplet began to fall under gravity. Simultaneously, the release of the acoustic compression led to a surface-tension-driven relaxation process, during which the droplet rebounded from its previously compressed ellipsoidal shape. This transient deformation is quantified in Fig. 3(*b*), which shows the evolution of the aspect ratio D_h/D_v as a function of time. Immediately after release, the droplet undergoes pronounced shape oscillations while falling, reflecting the competition between surface tension and inertia. As the oscillatory motion is progressively damped by viscous dissipation, the droplet gradually relaxes toward a spherical shape and maintains this geometry thereafter. These observations highlight an important consideration for experimental design. When specific initial droplet shapes or well-defined geometrical conditions are required for subsequent supercooled droplet experiments, an adequate relaxation time must be allowed after release from the acoustic levitator. Accounting for this transient shape recovery is essential to ensure controlled and repeatable initial conditions for droplet impingement and freezing studies using the developed freezing-levitation system.

3.2 Temperature Evolution of a Levitated Droplet in the Freezer System. When a droplet was generated by the syringe pump and introduced into the acoustic levitator, its initial temperature, T_d, was close to room temperature (approximately 20 °C). Once suspended inside the freezer chamber, the droplet was exposed to a cold ambient environment. The surrounding air temperature, T_{air}, was assumed to be uniform and equal to the measured chamber temperature, which remained within the range of −7.9 to −8.4 °C throughout the experiments. Under these conditions, heat transfer from the droplet to the surrounding air was dominated by convection, leading to a continuous decrease in T_d over time.

Figure 4 presents representative time-sequence infrared images illustrating the cooling process of both a DI water droplet and a tap water droplet while levitated in the acoustic field, where $t = 0$ s marks the onset of temperature measurement by the thermal camera. The infrared frames for the two cases were selected so that the comparison is made at the same time instants, allowing a direct comparison of the thermal evolution to highlight the distinct cooling behaviors in each case. The DI water droplet, initially at 11.5 °C, cooled to below 0 °C quickly (within 60 s) without freezing. After that, due to the smaller temperature difference between the droplet and the surrounding air, the heat convection rate was reduced, leading to a much slower cooling rate of the droplet from $t = 60$ s to $t = 500$ s in Fig. 4(*a*), which reflects the thermal equilibration of the droplet with the surrounding environment. It should be noted that, no nucleation or recalescence event was observed throughout this cooling process, indicating that the droplet remained in the liquid supercooled state at temperatures well below its equilibrium freezing point.

In contrast, while the tap water droplet experienced a similar cooling process from $t = 0$ s to $t \approx 200$ s, i.e., initially a rapid cooling stage followed by slower cooling, an increase in droplet temperature was observed, as can be seen at $t = 270$ s in Fig. 4(*b*). This abrupt temperature rise indicates the release of latent heat of fusion associated with spontaneous ice nucleation and recalescence. Following this event, the droplet temperature remained nearly constant at a temperature close to the equilibrium freezing temperature, see $t = 368.8$ s in Fig. 4(*b*). During this period, droplet was in the form of ice/water mixture, undergoing a progressive solidification process. Then, at around $t = 500$ s, it is seen that the droplet temperature decreased again and approached the surrounding temperature of approximately −7.5 °C.

These thermal behaviors were found to be repeatable across repeated trials. It was found that the tap water droplet consistently exhibited recalescence at $t = 240 \pm 60$ s, while no recalescence event was observed for the DI water droplet during the entire cooling period, up to 30 min. The different thermal histories observed for DI water and tap water droplets highlight the influence of impurities on nucleation behavior, while demonstrating that the developed system is capable of capturing the complete thermal evolution of droplets during supercooling, recalescence, and freezing.

Accurate prediction of T_d as a function of cooling time is essential for generating supercooled droplets with prescribed degrees of supercooling. To this end, Newton's law of cooling for free convection around a spherical object was employed to model the droplet temperature evolution

$$T_d(t) = T_{\text{air}} + (T_0 - T_{\text{air}})\exp^{\left(\frac{-t}{\tau}\right)} \quad (11)$$

Here $T_d(t)$ is the temperature of the droplet at a given cooling time t, T_{air} is the temperature of the surrounding air in the freezer, T_0 is the initial temperature of the droplet immediately after it is generated in the acoustic levitator, and $\tau = \frac{\rho C_p V}{hA}$ is the characteristic thermal time constant. In this framework, the droplet temperature, $T_d(t)$, decays exponentially toward the ambient air temperature, T_{air}, with the cooling rate governed by the characteristic thermal time constant. A key assumption of this model is that the droplet can be treated as isothermal at any given time, such that its temperature is spatially uniform and varies only with time. This assumption is justified by evaluating the Biot number (Bi), which compares internal thermal resistance to external convective resistance. In this study, the Biot number was estimated to be

$$B_i = \frac{hL_c}{k} = 0.024 < 0.1 \quad (12)$$

where $L_c \approx 5.0 \times 10^{-4}$m, $k \approx 0.58$ W/m·K and an estimated heat-transfer coefficient $h \approx 29$ W/m^2·K. Since acoustic streaming may increase the effective external heat transfer in the levitator, a sensitivity analysis was carried out for $h = 20$–80 W/m^2·K, which gives Bi ≈ 0.017–0.067. Thus, even under an elevated-h estimate, the Biot number remains below the conventional lumped-capacitance limit of 0.1, confirming the validity of the lumped-capacitance approximation. The lumped-capacitance approximation is applied here only to the prenucleation cooling stage as a first-order estimate of the droplet thermal response. The heat transfer coefficient in the model was determined using established Nusselt number correlations for free convection from a sphere [19,20]. This theoretical framework provides a quantitative

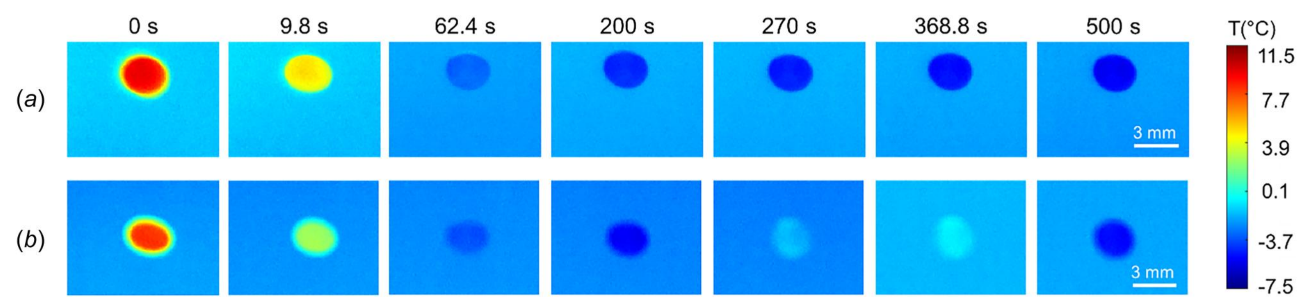

Fig. 4 Time-sequence infrared images of acoustically levitated droplet cooling in a freezer: (*a*) cooling of the DI water droplet and (*b*) cooling of a tap water droplet

description of the droplet cooling rate by linking heat dissipation to the temperature difference between the droplet and the surrounding air. It should be noted, however, that once nucleation occurs, the droplet thermal behavior becomes considerably more complex due to latent heat release, recalescence, internal temperature gradients, and the propagation of a moving phase front during solidification. These effects are not captured by the present lumped-capacitance model.

Figure 5 compares the experimentally measured temperature evolution of levitated DI water and tap water droplets, revealing different thermal behaviors associated with their freezing characteristics. Although both droplets initially cool from near room temperature toward the ambient freezer temperature, following a similar monotonic cooling trend, their subsequent temperature histories diverge markedly.

The tap water droplet exhibits a clear and identifiable recalescence event. After an initial cooling phase in which the droplet temperature decreases continuously, a sudden temperature rise is observed, indicating the release of latent heat of fusion associated with the onset of ice nucleation. This transient warming peak is a characteristic signature of freezing in supercooled water droplets and confirms that nucleation and solidification occurred. Following recalescence, the droplet temperature remains approximately at $-2\,^{\circ}\mathrm{C}$ during the solidification stage. Once freezing is complete, the temperature decreases again as the fully frozen droplet continues to dissipate heat to the surrounding air, ultimately stabilizing near $-7\,^{\circ}\mathrm{C}$ as thermal equilibrium with the ambient environment is approached. The freezing behavior of the tap water droplet is captured by high-speed imaging included in Fig. 5. An image acquired prior to the recalescence event shows a transparent droplet characteristic of the liquid phase, whereas an image captured after recalescence shows an opaque appearance, confirming ice formation following nucleation.

In contrast, the DI water droplet follows a smooth and uninterrupted cooling trend throughout the entire measurement period. No abrupt temperature increase or recalescence event is observed, indicating that the droplet remains in a metastable supercooled liquid state. Its temperature decreases gradually and eventually stabilizes in a similar low-temperature range as the tap water droplet, but without the distinctive thermal signature of a phase transition.

Based on the observed temperature evolution, the freezing process of the tap water droplet can be divided into several distinct stages. Initially, the droplet enters a supercooled stage, during which its temperature decreases below $0\,^{\circ}\mathrm{C}$ without any phase change. This is followed by a recalescence stage, marked by the onset of ice formation, during which latent heat release causes a transient temperature rise. Subsequently, the droplet undergoes a freezing stage, in which solidification progresses, followed by a solid cooling stage, where the fully frozen droplet cools toward the ambient freezer temperature. These stages are consistent with established descriptions of supercooled droplet freezing and demonstrate the capability of the present system to resolve the complete thermal history of droplet freezing.

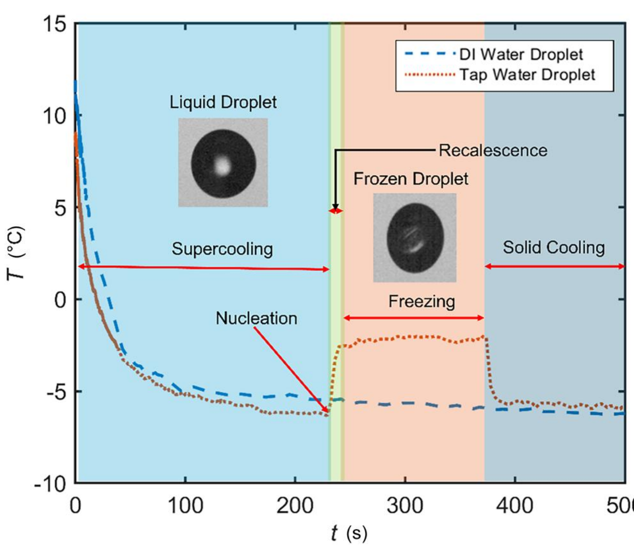

Fig. 5 Time-dependent temperature evolution of the acoustically levitated droplets during cooling in the freezing-levitator system

3.3 Effects of Supercooling on Droplet Impinging/Freezing Dynamics and Thermal Behavior.

To elucidate the effects of supercooling on droplet impingement and freezing dynamics, as well as the associated thermal behavior during the freezing process, both high-speed imaging and infrared thermography were employed. These complementary diagnostics enabled comprehensive characterization of the droplet morphological evolution during impact and its transient thermal response during phase change, i.e., freezing. Although both measurement techniques were applied in each experimental case, the high-speed camera and the infrared thermal camera were not perfectly synchronized on a frame-by-frame basis, mainly because of the substantial differences in their operating frame rates and the different time scales associated with the impingement hydrodynamics and freezing thermal processes. However, both cameras were initiated using a common trigger signal, so that the high-speed image and infra red image recordings shared the same nominal start time. In the present study, high-speed imaging was operated at much higher frame rate, i.e., 10,000 fps, over short durations to resolve the rapid droplet deformation and spreading immediately after impact, while infrared thermography was operated at a lower frame rate, i.e., 200 fps, but over longer time windows to capture the comparatively slower temperature evolution associated with cooling, nucleation, recalescence, and solidification. This measurement strategy allows both the fast hydrodynamic response and the slower thermal behavior to be adequately resolved, while recognizing that exact one-to-one temporal correspondence between individual optical and infrared frames is not available.

3.3.1 Morphological Evolution of the Droplets During Impact Freezing.

Figure 6 illustrates a comparison of the morphological evolutions of a supercooled droplet and a nonsupercooled (room-temperature) water droplet upon impingement on a cold hydrophilic surface (of $\sim -8\,^{\circ}\mathrm{C}$). The time-sequence images capture the droplet deformation from the moment of initial contact through the spreading and subsequent receding stages, highlighting the distinct impact and freezing behaviors exhibited by the two droplets.

Figure 6 compares the morphological evolution of supercooled and nonsupercooled droplets impacting a hydrophilic surface. Figure 6(*a*) shows the side-view hydrodynamic evolution of a representative supercooled droplet captured using high-speed imaging. At the moment of contact, $t = 0$ ms, the droplet remains nearly perfectly spherical, indicating that it falls without appreciable deformation after being released from the acoustic levitator inside the freezer. Upon contacting the hydrophilic substrate at $t \approx 0.6$–1.1 ms, the droplet spreads rapidly under inertial force, forming a thin radially expanding sheet, commonly referred to as a lamella. No splashing or secondary droplet formation is observed, consistent with the relatively low Weber number impact outcome and the hydrophilic nature of the substrate. By $t \approx 2.2$ ms, the droplet reaches its maximum spreading diameter and adopts a flattened pancake-like morphology, similar to those observed in the previous research [27]. The spreading process remains smooth and axisymmetric. At approximately $t \approx 3.1$ ms, the droplet begins to retract as surface tension acts to minimize the interfacial area. However, this retraction is abruptly arrested by the onset of freezing. By $t \approx 14$ ms, no further visible change in droplet shape is observed in the high-speed images, indicating that the droplet motion has been effectively arrested. Consequently, the droplet does not rebound or retract further but instead remains in a flattened configuration, which

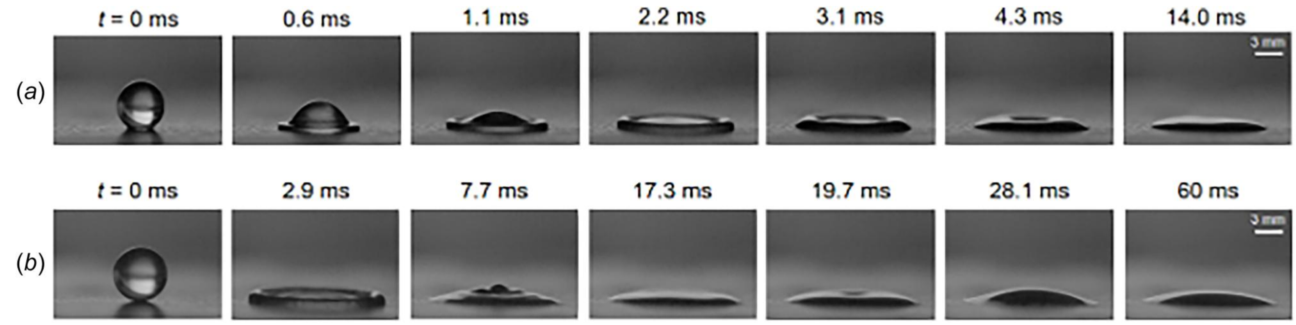

Fig. 6 Supercooled droplet impact on a hydrophilic surface. (*a*) Time-dependent shape change of the supercooled droplet. (*b*) Time-dependent shape change of the nonsupercooled droplet. Different time instants are shown to highlight the most significant stages in each case. The supercooled droplet shows early arrest of retraction associated with rapid postimpact freezing, while the nonsupercooled droplet undergoes continued capillary-driven recoil and relaxation before freezing.

is typical behavior for a supercooled droplet, i.e., an early onset of nucleation and solidification following impact.

The impact and spreading dynamics of a nonsupercooled (room-temperature) water droplet on the same cold hydrophilic surface are shown in Fig. 6(*b*). At $t = 0$ ms, corresponding to the instant of initial contact with the substrate, the droplet remains spherical. Immediately after impact, the droplet undergoes rapid inertial spreading. By $t = 2.9$ ms, a thin lamella has formed and expanded radially outward. Following maximum spreading, surface tension becomes the dominant restoring force, driving droplet retraction. By $t = 7.7$ ms, the retraction process is almost completed, and a slight upward bulge is observed at the droplet center, indicating the onset of capillary-driven recoil. As time progresses to $t = 17.3$–19.7 ms, the droplet continues to relax toward equilibrium. During this stage, a secondary retraction is evident in the central region, where upward liquid motion from beneath the droplet toward the free surface can be observed, reflecting internal flow redistribution following impact. By $t = 28.1$ ms, the droplet assumes a flattened but stable shape, indicating that the primary retraction process has concluded. At the final observed stage, $t = 60$ ms, the droplet remains slightly flattened with smooth rounded edges and a reduced height, consistent with a fully relaxed liquid droplet on a hydrophilic surface. In contrast to the supercooled droplet case, no abrupt arrest of motion is observed, as the absence of rapid freezing allows the droplet to complete its inertial-capillary relaxation process.

The qualitative observations from the high-speed image sequences in Fig. 6 were further quantified using the image processing methodology described in Sec. 2.5. Key droplet geometric parameters, including the initial droplet diameter (D_d), the spreading diameter (D), and the droplet height on the substrate (H) were extracted from each frame. To enable direct comparison between droplets of slightly different initial sizes, both D and H were normalized by D_d. Figure 7 shows the temporal evolutions of the normalized spreading diameter (D/D_d) and normalized height (H/D_d) for both the supercooled and nonsupercooled droplets.

As shown in Fig. 7(*a*), the normalized spreading diameter, D/D_d, for both the supercooled and nonsupercooled droplets follows nearly identical temporal trajectories during the initial impact stage, with both cases reaching a similar maximum spreading ratio within the first 0.04 ms after contact. This close agreement is consistent with previous studies [26], which have shown that variations in droplet temperature, and the associated changes in viscosity, exert only a minor influence on the maximum spreading behavior. During this early stage, droplet deformation is dominated by inertial forces balanced by capillary resistance, while viscous effects remain comparatively small. As a result, the impact dynamics are largely insensitive to differences in temperature and liquid microstructure. This explains why the supercooled and nonsupercooled droplets in the present experiments exhibit nearly identical maximum spreading, despite their substantially different initial thermal states. Similar conclusions have been reported for droplet impacts on subcooled surfaces, where maximum spreading is primarily inertia-controlled and only weakly dependent on temperature or phase-change effects [28].

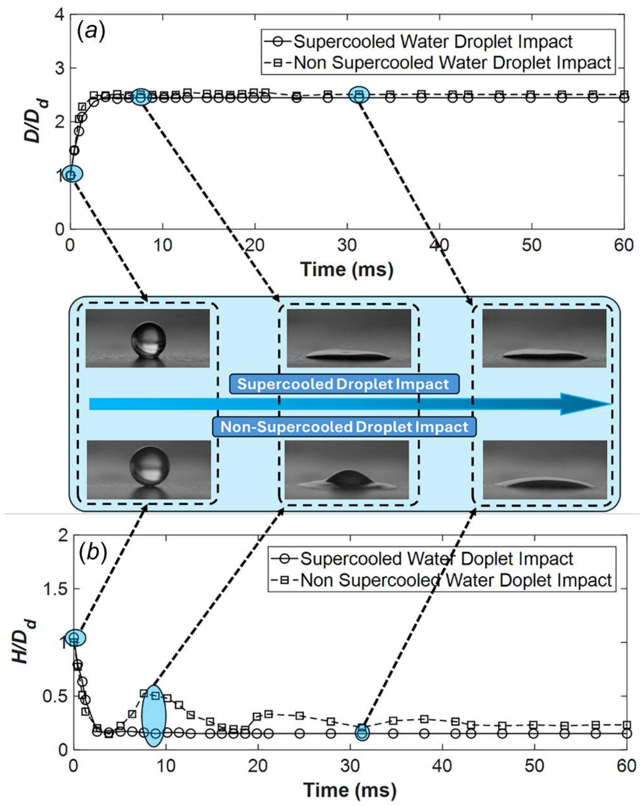

Fig. 7 Evolution of impinging supercooled droplets on hydrophilic substrates over time: (*a*) normalized spreading diameter D/D_d of the droplet as a function of time and (*b*) normalized height H/D_d of the droplet as a function of time

In contrast, the normalized droplet height evolution, H/D_d, shown in Fig. 7(*b*) reveals a clear divergence between the two cases. After the initial spreading phase, the nonsupercooled droplet undergoes pronounced retraction, resulting in a substantial increase in droplet height as the liquid recoils toward the center. By comparison, the supercooled droplet remains significantly flatter and exhibits only weak retraction. This behavior is consistent with that reported in [26], which demonstrated that viscous effects become increasingly important during the retraction phase, when surface energy is converted back into kinetic energy. In the supercooled droplet, the higher viscosity enhances viscous dissipation during spreading, reducing the amount of recoverable energy available for retraction. More importantly, nucleation occurs early in the post-impact stage, initiating solidification from the bottom of the droplet.

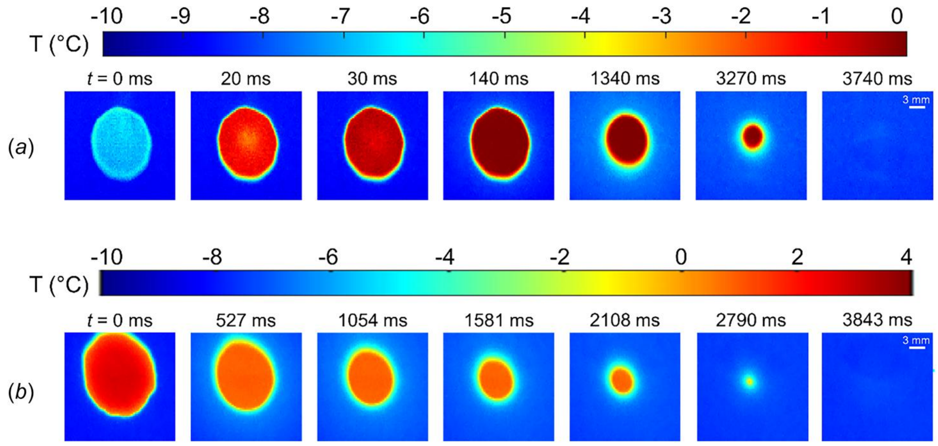

Fig. 8 Transient temperature evolutions of the droplets impact on a hydrophilic surface: (*a*) time-dependent temperature evolution of the supercooled droplet and (*b*) time-dependent temperature evolution of the nonsupercooled droplet

Consequently, retraction is suppressed, leading to a reduced recovery in droplet height and a flattened final morphology.

3.3.2 Transient Temperature Evolution of the Droplets During Impact Freezing. Figure 8 presents time-sequence infrared images illustrating the transient temperature evolution of both supercooled and nonsupercooled droplets upon impact with the hydrophilic surface. These thermal images provide direct insight into the thermal behaviors of the droplets during the freezing phase-change processes.

The thermal image sequence in Fig. 8(*a*) illustrates the transient temperature evolution of a supercooled droplet immediately following impact. At $t = 0$ ms, the droplet appears uniformly cold, confirming that it is well supercooled prior to contacting the substrate. Shortly after impact, a rapid increase in droplet temperature is observed, indicating the onset of freezing triggered by substrate contact. As time progresses, the droplet continues to warm, and by $t = 140$ ms, the droplet temperature becomes increasingly uniform and shifts toward higher temperatures, approaching 0 °C. This transient temperature increase process reflects the release of latent heat of fusion during nucleation and subsequent crystal growth.

At $t = 1340$ ms, the droplet begins to cool progressively from the periphery inward, indicating the progression of solidification. This cooling phase indicates that the majority of latent heat has been released and that the frozen droplet is dissipating heat to the surrounding cold environment. By $t = 3740$ ms, the droplet temperature becomes nearly indistinguishable from the background, suggesting that freezing is complete and that thermal equilibrium with the ambient freezer environment has been reached.

The thermal image sequence in Fig. 8(*b*) illustrates the temperature evolution of a nonsupercooled droplet following impact on the hydrophilic surface. At $t = 0$ ms, corresponding to the moment of impact, the droplet appears relatively warm, with an initial temperature of approximately 2 °C, making it clearly distinguishable from the colder substrate in the background. Immediately after impact, the droplet begins to lose heat to the substrate and surrounding air. By $t = 527$ ms, the droplet temperature has decreased noticeably, although a warm region remains visible in the thermal images. At $t = 1054$–1581 ms, the warm area contracts toward the droplet center, indicating continued heat dissipation and cooling. As time progresses to $t = 2108$ ms and 2790 ms, the majority of the droplet periphery has cooled to near the substrate temperature, leaving only a small warm region near the center. Finally, by $t = 3843$ ms, the droplet becomes nearly indistinguishable from the background in the thermal field, indicating that it has cooled sufficiently and reached thermal equilibrium with the cold substrate and ambient environment. Unlike the supercooled droplet, no abrupt temperature increase or nonmonotonic thermal behavior is observed, confirming that the nonsupercooled droplet undergoes a smooth sensible-heat-dominated cooling process.

To quantitatively compare the thermal response of droplets upon impact, time-resolved temperature profiles for both the supercooled and nonsupercooled droplets were extracted from the infrared measurements. Figure 9 presents the complete temperature histories from the moment of impact until each droplet approaches the substrate temperature within the freezer environment.

The temperature profile of the nonsupercooled droplet indicates that, at the moment of impact, its temperature is approximately 2 °C, consistent with the thermal images shown in Fig. 8(*b*). Following impact, the droplet undergoes a gradual and monotonic cooling process as heat is transferred to the colder substrate and surrounding air. As time progresses, the temperature continues to decrease steadily, reaching approximately –6 °C at $t = 3.8$ s, after which it remains nearly constant until $t = 4.5$ s, indicating that the droplet has approached thermal equilibrium with the freezer environment. In contrast, the supercooled droplet begins at a substantially lower initial temperature of approximately –6.5 °C prior to impact. Immediately after contact with the substrate, its temperature rises sharply and reaches a peak near 0 °C, as shown in Fig. 9. This transient temperature increase is a direct consequence of latent heat

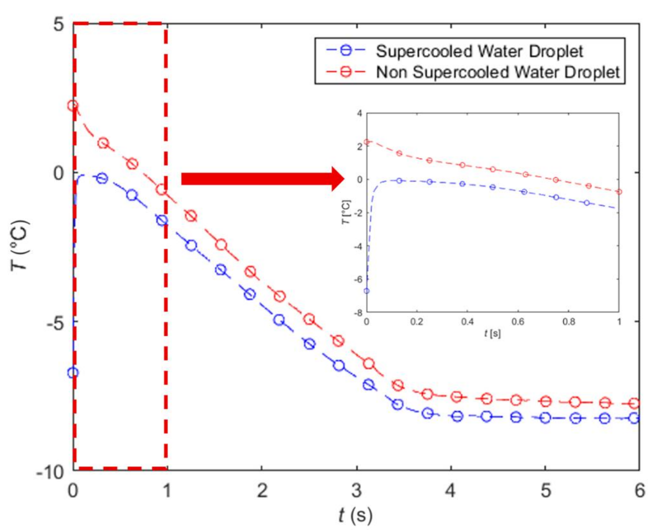

Fig. 9 Transient temperature profile of supercooled and non-supercooled water droplets with an inset of the initial timescale

release associated with impact-triggered nucleation and freezing. Following this brief recalescence event, the droplet temperature decreases rapidly, and by $t = 3.7$ s, it has cooled to approximately –8 °C, where it remains for the remainder of the observation period.

4 Conclusions

In this study, a freezing-levitation system was developed to generate supercooled droplets with controlled, repeatable supercooling levels, and its feasibility was experimentally demonstrated. In the proposed configuration, droplets were generated through a needle and introduced into an acoustic levitator installed inside a freezing chamber. The acoustic standing-wave field enabled stable, contact-free droplet suspension in air, eliminating heterogeneous nucleation associated with physical supports. During levitation, droplets were cooled solely through heat exchange with the surrounding cold environment, allowing their temperature to be regulated by controlling the levitation duration. Both high-speed imaging and infrared thermography were employed to quantify the dynamic and thermal evolution of levitated droplets. The measurements revealed distinct cooling behaviors for de-ionized and tap-water droplets, with tap water exhibiting a clear recalescence event associated with impurity-triggered nucleation. In contrast, de-ionized water remained supercooled over the same cooling period. In practice, a water droplet with a diameter of approximately 3 mm required a period of five minutes of levitation to reach a supercooled state under the present experimental conditions. These results demonstrate the system's ability to produce supercooled droplets with prescribed degrees of supercooling reliably.

The freezing-levitation platform was further used for impact experiments on a hydrophilic substrate. For the present release height of 15.4 cm, the impact velocity was approximately 1.74 m/s, corresponding to $\mathrm{We} \approx 120$, $\mathrm{Re} \approx 2.9 \times 10^3$, $\mathrm{Bo} \approx 1.2$, and $\mathrm{Oh} \approx 0.012$. Under these conditions, both supercooled and non-supercooled droplets exhibited similar early spreading behavior, indicating that the initial impact stage was primarily governed by inertia-capillary forces and relatively insensitive to the initial droplet temperature. Clear differences emerged during the later stage: the supercooled droplet underwent rapid post-impact freezing, which suppressed retraction and produced an early flattened morphology, whereas the nonsupercooled droplet completed retraction, showed upward motion near the droplet center, and froze only after hydrodynamic motion had substantially completed. The significant contribution of this work is the development of a simple, effective platform for the contact-free generation of supercooled droplets, particularly with respect to the actual degree of supercooling prior to impact, thereby overcoming a major experimental limitation in supercooled-droplet research. This study also provides direct experimental evidence of the transition of the generated supercooled droplet from inertia-capillary impact dynamics to freezing-dominated post-impact behavior.

Conflict of Interest

The authors declare no conflicts of interest.

Funding Data

- U.S. Department of Energy, Office of Science, Office of Fusion Energy Sciences (Award No. DE-SC0024663; Funder ID: 10.13039/100006207).

Nomenclature

A = surface area of the droplet
Bi = Biot number (dimensionless)
C = counts from infrared images
C_p = specific heat capacity of the droplet
D = spreading diameter of the droplet on the substrate
D_d = initial diameter of the droplet
D_h = horizontal diameter of the droplet
D_v = vertical diameter of the droplet
F_g = weight of the droplet
g = acceleration due to gravity
H = Height of the droplet on the substrate
H = convective heat transfer coefficient
K = thermal conductivity of the droplet
L_c = characteristic length of the droplet
m = mass of the droplet
t = time
T_{air} = temperature of the surrounding air
T_d = temperature of the droplet
T_0 = initial temperature of the droplet
U_d = impact velocity of the droplet
V = volume of the droplet
γ = surface tension coefficient
θ = static contact angle
μ = viscosity
P = density
τ = thermal time constant of the droplet

References

[1] Jung, S., Tiwari, M. K., Doan, N. V., and Poulikakos, D., 2012, "Mechanism of Supercooled Droplet Freezing on Surfaces," Nat. Commun, **3**(1), p. 615.
[2] Johnson, D. A., and Hallett, J., 1968, "Freezing and Shattering of Supercooled Water Drops," Q. J. R. Meteorolog. Soc., **94**(402), pp. 468–482.
[3] Tavakoli, F., Davis, S. H., and Kavehpour, H. P., 2015, "Freezing of Supercooled Water Drops on Cold Solid Substrates: Initiation and Mechanism," J. Coat. Technol. Res, **12**(5), pp. 869–875.
[4] Blake, J., Thompson, D., Raps, D., and Strobl, T., 2015, "Simulating the Freezing of Supercooled Water Droplets Impacting a Cooled Substrate," AIAA J., **53**(7), pp. 1725–1739.
[5] Liu, Y., Wang, T., Song, Z., and Chen, M., 2022, "Spreading and Freezing of Supercooled Water Droplets Impacting an Ice Surface," Appl. Surf. Sci, **583**, p. 152374.
[6] Zhang, H., Lazo, J. A., Bin Sarwar, M. D. S., and Liu, Y., 2025, "Revealing the Dynamic and Thermal Behaviors of Supercooled Droplet Impinging on Surfaces With Varying Wettability," Soft Matter, **21**(45), pp. 8655–8668.
[7] Puffing, R. F. A., Peciar, M., and Hassler, W., 2013, "Instrumentation of an Icing Wind Tunnel Based on SAE Standards," Sci. Proc. Faculty Mech. Eng., Slovak Univ. Technol. Bratislava, **21**(1), p. 37.
[8] Hadizadeh, M. H., Pan, Z., and Azamat, J., 2022, "A New Insight Into the Interaction of Hydroxyl Radical With Supercooled Nanodroplet in the Atmosphere," J. Mol. Liq., **359**, p. 119261.
[9] Murray, B. J., O'Sullivan, D., Atkinson, J. D., and Webb, M. E., 2012, "Ice Nucleation by Particles Immersed in Supercooled Cloud Droplets," Chem. Soc. Rev., **41**(19), pp. 6519–6554.
[10] Zhang, R., Hao, P., Zhang, X., and He, F., 2018, "Supercooled Water Droplet Impact on Superhydrophobic Surfaces With Various Roughness and Temperature," Int. J. Heat Mass Transfer, **122**, pp. 395–402.
[11] Yan, X., Au, S. C. Y., Chan, S. C., Chan, Y. L., Leung, N. C., Wu, W. Y., Sin, D. T., et al., 2024, "Unraveling the Role of Vaporization Momentum in Self-Jumping Dynamics of Freezing Supercooled Droplets at Reduced Pressures," Nat. Commun., **15**(1), p. 1567.
[12] Adachi, T., Daudah, D., and Tanaka, G., 2014, "Effects of Supercooling Degree and Specimen Size on Supercooling Duration of Erythritol," Isij Int., **54**(12), pp. 2790–2795.
[13] Ding, B., Wang, H., Zhu, X., Chen, R., and Liao, Q., 2019, "Water Droplet Impact on Superhydrophobic Surfaces With Various Inclinations and Supercooling Degrees," Int. J. Heat Mass Transfer, **138**, pp. 844–851.
[14] Wei, B.-J., Shi, L.-K., Gao, S.-R., Shi, S.-H., Liu, Z., Wang, Y.-F., Yang, Y.-R., and Wang, X.-D., 2025, "Experimental Study on Dynamics and Freezing Characteristics of Droplet Impact on Supercooled Surfaces," Int. J. Therm. Sci., **213**, p. 109811.
[15] Wang, L., Wang, F., Bian, P., and Liu, H., 2025, "Maximum Spreading and Freezing of Water Droplet Impacting on Ice Surface," Appl. Therm. Eng., **274**, p. 126547.
[16] Yu, H., Zhou, X., Wang, H., Zhang, Q., Zhu, X., Ding, Y. D., Chen, R., and Liao, Q., 2024, "Effect of Temperature Difference Between Impinging Droplet and Cold Superhydrophobic Surface on Its Dynamic Behavior," Exp. Therm. Fluid Sci., **150**, p. 111049.
[17] Gao, S.-R., Shi, S.-H., Wang, Y.-X., Jia, Q.-H., Wei, B.-J., Yang, Y.-R., and Wang, X.-D., 2025, "Freezing Property of a Droplet Impacting Supercooled Hydrophilic Surfaces," Phys. Fluids, **37**(3), p. 037110.
[18] Yarin, A. L., Pfaffenlehner, M., and Tropea, C., 1998, "On the Acoustic Levitation of Droplets," J. Fluid Mech., **356**, pp. 65–91.
[19] Lieber, C., Autenrieth, S., Schönewolf, K.-Y., Lebanoff, A., Koch, R., Smith, S., Schlinger, P., and Bauer, H.-J., 2024, "Application of Acoustic Levitation for Studying Convective Heat and Mass Transfer During Droplet Evaporation," Int. J. Multiphase Flow, **170**, p. 104648.
[20] Winterton, R. H. S., 1999, "Newton's Law of Cooling," Contemp. Phys, **40**(3), pp. 205–212.

[21] White, F. M., and Xue, H., 2003, *Fluid Mechanics*, Vol. 3, McGraw-Hill, New York.
[22] Yang, M.-W., and Lin, S.-Y., 2003, "A Method for Correcting the Contact Angle From the $\theta/2$ Method," Colloids Surf. A Physicochem. Eng. Asp, **220**(1–3), pp. 199–210.
[23] Andrade, M. A. B., Pérez, N., and Adamowski, J. C., 2018, "Review of Progress in Acoustic Levitation," Braz. J. Phys., **48**(2), pp. 190–213.
[24] Zang, D., Yu, Y., Chen, Z., Li, X., Wu, H., and Geng, X., 2017, "Acoustic Levitation of Liquid Drops: Dynamics, Manipulation and Phase Transitions," Adv. Colloid Interface Sci, **243**, pp. 77–85.
[25] Zhang, H., Zhang, X., and Liu, Y., 2025, "A Novel Freezing-Sublimation-Based Method for Enhancing Deposition Uniformity of Colloidal Particles in Inkjet 3D Printing: A Proof-of-Concept Study," Colloids Surf. A Physicochem. Eng. Asp., **713**, p. 136513.
[26] Di, W., Zhang, Z., Li, L., Lin, K., Li, J., Li, X., Binks, B. P., Chen, X., and Zang, D., 2018, "Shape Evolution and Bubble Formation of Acoustically Levitated Drops," Phys. Rev. Fluids, **3**(10), p. 103606.
[27] Lee, C. P., Anilkumar, A. V., and Wang, T. G., 1991, "Static Shape and Instability of an Acoustically Levitated Liquid Drop," Phys. Fluids A: Fluid Dyn., **3**(11), pp. 2497–2515.
[28] Može, M., Shang, Y., Jereb, S., Kovač, N., Štucin, M., Štrus, T., Rodič, P., Zupančič, M., Vetrano, M. R., and Golobič, I., 2025, "Surface Morphology Effects on Droplet Spreading and Rebound Dynamics on Subcooled Superhydrophobic Surfaces," Scientific Reports, **15**(1), p. 29530.